

Mitigating Scattering in a Quantum System Using Only an Integrating Sphere

Zhenfei Jiang^{1,2}, Tian Li^{3,4,*}, Matthew L. Boone^{1D},³ Zhenhuan Yi^{1D},^{1,2,†} Alexei V. Sokolov^{1D},^{1,2,5}
Girish S. Agarwal,^{1,2,6} and Marlan O. Scully^{1D},^{1,2,7}

¹*Institute for Quantum Science and Engineering, Texas A&M University, College Station, Texas 77843, USA*

²*Department of Physics and Astronomy, Texas A&M University, College Station, Texas 77843, USA*

³*Department of Chemistry and Physics, University of Tennessee at Chattanooga, Chattanooga, Tennessee 37403, USA*

⁴*UTC Research Institute, University of Tennessee at Chattanooga, Chattanooga, Tennessee 37403, USA*

⁵*Department of Physics, Baylor University, Waco, Texas 76798, USA*

⁶*Department of Biological and Agricultural Engineering, Texas A&M University, College Station, Texas 77843, USA*

⁷*Department of Electrical and Computer Engineering, Princeton University, Princeton, New Jersey 08540, USA*

(Received 21 May 2024; revised 10 July 2024; accepted 19 August 2024; published 13 September 2024)

Strong quantum correlated sources are essential but delicate resources for quantum information science and engineering protocols. Decoherence and loss are the two main disruptive processes that lead to the loss of nonclassical behavior in quantum correlations. In quantum systems, scattering can contribute to both decoherence and loss. In this work, we present an experimental scheme capable of significantly mitigating the adverse impact of scattering in quantum systems. Our quantum system is composed of a two-mode squeezed light generated with the four-wave-mixing process in hot rubidium vapor and a scatterer is introduced to one of the two modes. An integrating sphere is then placed after the scatterer to recollect the scattered photons. We use mutual information between the two modes as the measure of quantum correlations and demonstrate a 47.5% mutual information recovery from scattering, despite an enormous photon loss of greater than 85%. Our scheme is the very first step toward recovering quantum correlations from disruptive random processes and thus has the potential to bridge the gap between proof-of-principle demonstrations and practical real-world implementations of quantum protocols.

DOI: 10.1103/PRXQuantum.5.030351

I. INTRODUCTION

Quantum information science and engineering (QISE) harnesses the principles of quantum mechanics to manipulate and process information, leading to groundbreaking advancements in computing, communication, and sensing [1]. Nevertheless, quantum correlations, the cornerstone of QISE, are inherently fragile. They are very susceptible to disruptive processes such as decoherence and loss, resulting in the loss of their nonclassical forms of behavior [2]. Therefore, mitigating the adverse effects of those disruptive processes on quantum correlations in quantum

systems is highly beneficial for the implementations of QISE protocols [3].

Among those well-studied quantum systems, squeezed states of light have been used as reliable quantum resources in various QISE protocols [4–11], particularly those devised in the continuous-variable (CV) regime [12]. Here, we use a two-mode squeezed state of light generated with the four-wave-mixing (FWM) process in hot rubidium vapor as the quantum source to study mitigating the adverse effects of disruptive processes on quantum correlations. It is well understood that the squeezing level is equally reduced by linear loss, while optical group delay, e.g., the delay between the probe and the conjugate mode of our source due to the refractive-index difference, can be corrected electronically without affecting the squeezing. It is also worth noting that active shaping of the temporal wave package of the twin photons can revive entanglement by restoring quantum interference [13]. However, real-world applications, such as quantum sensing and imaging, often encounter absorption and random scattering. To simplify the model, we employ a scatterer to introduce

*Contact author: tian-li@utc.edu

†Contact author: yzh@tamu.edu

Published by the American Physical Society under the terms of the [Creative Commons Attribution 4.0 International license](#). Further distribution of this work must maintain attribution to the author(s) and the published article's title, journal citation, and DOI.

disturbance into the quantum system, because scattering can contribute to both decoherence and scattering loss. Mitigation is realized by simply recollecting scattered photons using an integrating sphere (IS).

We adopt mutual information (MI) as the information metric to measure quantum correlations [14]. The MI and its quantum counterpart, the quantum mutual information (QMI), are very effective tools in quantifying quantum correlations [15–17]. This metric provides a precise measure of the shared MI between two quantum systems, offering valuable insights into their quantum correlations. In fact, the QMI in bipartite Gaussian states in the CV regime has been employed to facilitate a coherent representation of information within quantum systems, thus fostering valuable applications in quantum information processing [18–21]. Since calculating the QMI for bipartite Gaussian states involves determining the covariance matrix and this work does not involve field-quadrature measurements, we therefore do not use the QMI as the measure of quantum correlations. Instead, we use Shannon entropy to calculate the MI [14] for our quantum system consisting of the two quantum correlated bright modes generated through the FWM process. Specifically, *the MI is calculated from the joint probability of the intensity fluctuations of the two modes*, which encapsulates the squeezed nature between them. A ground glass diffuser, acting as a photon scatterer, is mounted at the front aperture of an IS, which then collects the scattered photons and sends them through its back aperture to a photodetector. Using this scattering-mitigation scheme, we are able to recover 47.5% of the MI after a time delay of 32.7 ns, despite an enormous photon loss of greater than 85%. Due to the simplicity of our scheme, which only involves an IS, it can find many applications in QISE protocols where scattering is inevitable.

II. EXPERIMENT

The two-mode squeezed light used in this work is generated with the FWM process in an atomic ^{85}Rb vapor cell [4,15,22–25]. This squeezed-light-generation scheme has proven to be an effective way of producing quantum correlations [15,16,26–28]. The experimental setup and the respective ^{85}Rb atomic level structure are shown in Figs. 1(a) and 1(b). The atomic medium is pumped by a strong (approximately 500 mW) narrow-band continuous-wave (CW) laser at frequency ν_1 ($\lambda = 795 \text{ nm}$), with a typical line width $\Delta\nu_1 \sim 100 \text{ kHz}$. We apply an additional weak (from a few hundred microwatts to approximately 1 mW) coherent seed beam at frequency $\nu_p = \nu_1 - (\nu_{HF} + \delta)$, where ν_{HF} and δ are the hyperfine splitting in the electronic ground state of ^{85}Rb and the two-photon detuning, respectively, in Fig. 1(b) (further experimental details can be found in Ref. [4]). Two pump photons are converted into a pair of “twin” photons, namely, “probe ν_p ” and

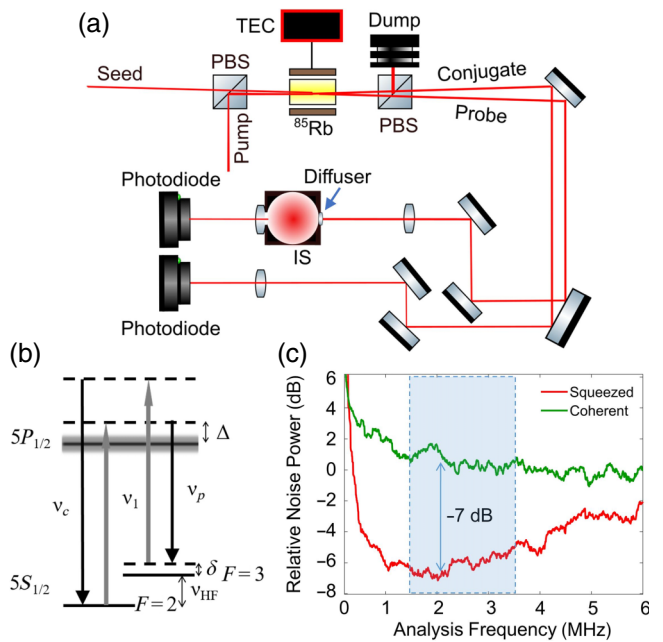


FIG. 1. (a) The experimental setup, in which a seeded ^{85}Rb vapor cell generates strong quantum correlated “twin” beams, i.e., the “probe” and “conjugate” beams, via FWM. A 5-cm-diameter integrating sphere (IS) is placed on the probe beam path and a “scatterer,” i.e., a 0.5-in.-diameter ground-glass diffuser, is placed at the entrance aperture of the IS. The focused probe beam is incident on the specular side of the diffuser. The other side (facing the IS) of the diffuser has 120 grits, which can produce near-spherical scattering patterns. A lens is attached to the exit aperture of the IS to collect escaped probe photons from IS and send them to a homemade photodetector. PBS, polarizing beam splitter; TEC, thermoelectric cooler. (b) The energy diagram of the D_1 transition of the ^{85}Rb atom. The optical transitions form a double- Λ configuration, where ν_1 , ν_p , and ν_c denotes the pump, probe, and conjugate frequencies, respectively, with $\nu_p + \nu_c = 2\nu_1$. The Doppler broadening is represented by the width of the excited state (gray). Δ and δ are the single- and two-photon detuning, respectively. ν_{HF} is the hyperfine splitting in the $5S_{1/2}$ state of ^{85}Rb . (c) A typical two-mode intensity-difference squeezing spectrum obtained by postprocessing the intensity fluctuations of the twin beams in software. The red and green curves denote the spectra of the squeezed and coherent beams, respectively. A squeezing level of 7 dB can be achieved on a daily basis. The shaded area from 1.5 MHz to 3.5 MHz is our region of interest for data analysis.

“conjugate ν_c ” photons, adhering to the energy conservation $2\nu_1 = \nu_p + \nu_c$ [see the level structure in Fig. 1(b)]. The photon-number fluctuations (i.e., the intensity fluctuations) of the probe and conjugate beams are strongly quantum correlated, as exhibited by the strong two-mode squeezing between them.

A typical squeezing spectrum, obtained by postprocessing the intensity fluctuations of the probe and conjugate beams in software, is shown in Fig. 1(c). The shot-noise limit (SNL), shown as the green curve in Fig. 1(c), is

measured by isolating the “seed” beam [a coherent beam, labeled as “Seed” in Fig. 1(a)] before it enters the ^{85}Rb cell. We split the beam using a half-wave plate and a polarizing beam splitter (PBS), ensuring that the two outputs of the PBS match the optical powers of the twin beams. These two resulting coherent beams are then directed into two photodetectors to register their intensity fluctuations. These detectors are home built and their photodiodes have a quantum efficiency greater than 92%. The intensity-fluctuation time traces are subtracted and then Fourier transformed in software to yield the noise power of the intensity difference between the two beams. This noise-power level serves as a measure of the SNL for the total optical power arriving at the two photodetectors. The SNL is expected to be independent of frequency, which is consistent with our observations within the bandwidth of the detection electronics, with a drop-off occurring above 10 MHz [not shown in Fig. 1(c)]. The red curve in Fig. 1(c) represents the noise power for the intensity difference between the probe and conjugate beams, showing a 7-dB reduction below the SNL.

Note that in this work, we are not measuring squeezing in field quadratures but, rather, in the intensity difference of a bipartite entangled state, which is generated through the FWM process in ^{85}Rb by converting two photons from a strong coherent pump beam into twin photons emitted into spatially separated probe and conjugate modes. This type of squeezing, also referred to as “*bright two-mode squeezing*,” results in a photon flux of the probe and conjugate beams ranging from 10^{13} to 10^{16} photons per second [29]. Although the generation of photons in each mode is random (i.e., thermal-like individually), there is a strong quantum correlation between the probe and conjugate modes in their intensity fluctuations, because the entangled photons are produced in pairs by the FWM process. This strong quantum correlation leads to the observed squeezing in the intensity difference of the probe and conjugate beams shown in Fig. 1(c).

Since the pump and the twin beams are cross-polarized, and thus after the cell, we use a Glan-Laser polarizing beam splitter with an approximately $2 \times 10^5 : 1$ extinction ratio for the pump polarization, to filter out the pump photons from the twin beams. The conjugate beam is then sent directly to the home-built photodetector, while the probe beam propagates through a scatterer, i.e., a 0.5-in.-diameter ground-glass diffuser (Thorlabs, DG05-120), with its polished side facing the beam. The other side of the scatterer is a medium-grit surface (120 grit), producing near-spherical scattering patterns. The scatterer is placed at the entrance aperture (also 0.5-in.-diameter) of a 5-cm-diameter IS (Thorlabs, IS200-4), with which almost all of the scattered photons can be confined inside. After the IS, a 1-in.-diameter lens with a 25-mm focal length is attached immediately after the exit aperture of the IS to collect those exiting photons and focus them to another laboratory-made

photodetector with a quantum efficiency similar to the conjugate photodiode. Due to repeated imperfect reflections of the scattered photons inside the IS with approximately 98% surface reflectivity, the optical power of the exiting photons is only approximately 14% of the probe input power.

We use an oscilloscope to record photocurrents from the photodetectors for postprocessing the quantum correlations in the photon-number fluctuations (i.e., intensity fluctuations) of the twin beams. Also note that since we are focused on the temporal quantum correlations in the total intensities of the twin beams, the polarization of the twin beams is not relevant to our study. The registered photocurrent (i.e., the oscilloscope trace of voltage versus time) of each detector consists of 4×10^6 points acquired at a sampling rate of 2.0 Gsamples/s for a total acquisition time of 2 ms. In the following, we use the MI formalism to describe the correlations of the twin beams and provide a theoretical model that explains our experimental observations quite well.

III. RESULTS

A. Mutual information of twin beams

The MI of the twin beams is calculated under two configurations: (i) the probe and conjugate beams are unobstructed and (ii) a combination of the scatterer and the IS is placed on the probe beam path, while the conjugate beam is unobstructed. The optical power of the probe beam before the scatterer is 5.9 mW, which reduces to 750 μW after passing the scatterer and being recollected by the IS, consisting of only 14% of the input probe power. In both configurations, the optical power of the conjugate beam is kept at 5.3 mW. The intensity fluctuations of the twin beams in configurations (i) and (ii) are shown in Figs. 2(a) and 2(b), respectively, where the *x* axis is time and the *y* axis is the digitization level of an 8-bit oscilloscope with a maximal value of $2^8 = 256$.

As can be seen in Fig. 2(a), when the twin beams are unobstructed, i.e., without the scatterer on the probe beam path, the temporal forms of behavior of the intensities of the twin beams are quite similar, even among very fine (i.e., high-frequency) fluctuating features. This indicates the existence of strong correlations between the unobstructed probe and conjugate beams beyond the classical-noise regime. In Fig. 1(c), the quantum correlations in the shot-noise-limited regime are manifested by more than 7 dB of intensity-difference squeezing. For configuration (ii), the level range of the probe intensity fluctuation shown in Fig. 2(b) is significantly reduced, along with the probe optical power, due to the proportionality between the variance and the mean. The level range of the intensity fluctuations of the conjugate beam stays the same. As can be seen in Fig. 2(b), the randomness introduced to the probe intensity fluctuations by the scatterer visibly

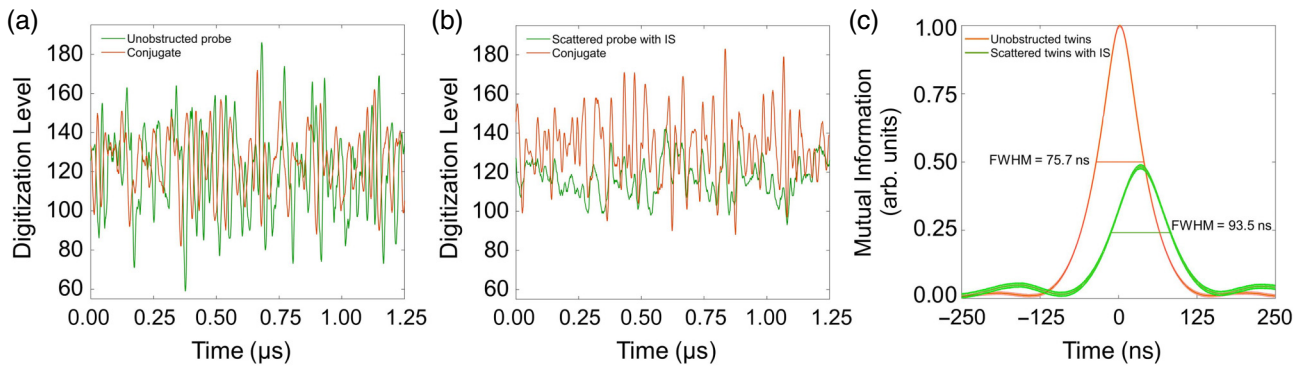


FIG. 2. (a),(b) The intensity fluctuations of the twin beams in (a) and (b) are for the experimental configurations described in the text as (i) and (ii), respectively. (c) The normalized MI of the twin beams as a function of the relative delay obtained by calculating Eq. (1) at every time-shift step of 0.5 ns. The red and green curves are the MI plots for configurations (i) and (ii), respectively. The shadow on each curve represents one standard deviation of averaging over ten pairs of intensity fluctuations.

breaks the intensity correlations in large time scales, i.e., classical correlations in the technical-noise regime. It also washes out the correlated fine fluctuating features, i.e., quantum correlations in the shot-noise regime, making the temporal behavior of the probe beam intensity appear to be smoother after traveling through the scatterer and the IS.

To compute the MI, the intensity fluctuations of the probe and conjugate beams are filtered in software by a band-pass filter from 1.5 MHz to 3.5 MHz, where the source has the best squeezing level, as shown in Fig. 1(c) by the shaded area of the squeezing spectrum. Despite the probe and conjugate fluctuations individually being random in nature, the fluctuations on one beam carry information about the fluctuations on the other. Therefore, correlated information is shared between the twin beams, even to the shot-noise level. We capture these correlations by calculating the MI between the intensity fluctuations of the twin beams using the equation [1]

$$I(p; c) = \sum_1^{N_p} \sum_1^{N_c} P(p, c) \log_2 \frac{P(p, c)}{P(p)P(c)}, \quad (1)$$

where $P(p, c)$ is the joint probability distribution obtained from a two-dimensional intensity-fluctuation histogram by binning the intensity fluctuations of the probe and conjugate beams individually, i.e., *binning the intensity fluctuations on the y axes* in Figs. 2(a) and 2(b). $P(p)$ and $P(c)$ are the marginal probabilities of the intensity fluctuations of the probe and conjugate beams, respectively. N_p and N_c are the number of bins for the two intensity fluctuations. We then can obtain the MI as a function of time by shifting the two intensity fluctuations relative to each other along the x axis by a step of 0.5 ns (i.e., the sampling resolution of the oscilloscope) and calculating Eq. (1) at each time shift. Note that in contrast to the calculation of the QMI,

which would involve the knowledge of both quadratures of the two fields, Eq. (1) only yields the MI in the amplitude quadrature.

The number of bins can vary depending on the dynamic range of the intensity fluctuations, i.e., the number of digitization levels that the fluctuations occupy. With a finite dynamic range, the larger the number of bins, the finer the bin size will be and thus we are able to resolve fine and/or high-frequency fluctuations. As the dynamic range of most of the intensity fluctuations is within 100 digitization levels, we thus pick $N_p = N_c = 100$ throughout our data analysis for obtaining the histograms.

The MI of the twin beams as a function of the time shift [i.e., Eq. (1) calculated at each time-shift step] for cases (i) and (ii) is presented in Fig. 2(c) by the red and green curves, respectively. Each curve is the average over ten pairs of intensity fluctuations. Note that error bars representing one standard deviation are also shown on the graph, although they are too small to be readily discerned. We normalize the peak height of the MI in case (i) to unity; it appears to look like a Gaussian profile with a full width at half maximum (FWHM) of 75.7 ns. With this normalization, in case (ii), the peak height of the MI is reduced to 0.475, with a broadened FWHM of 93.5 ns. In addition to the Gaussian-profile change, the peak position of the green curve is also delayed by $\tau_0 = 32.7$ ns with respect to the peak position of the red curve. This time delay τ_0 can be comprehended as the “memory time” of the IS, implying that 47.5% of the input (i.e., unobstructed) MI can be stored in the IS for $\tau_0 = 32.7$ ns.

We also investigate the configuration in which *only the scatterer is present* on the probe beam path. We use the same experimental setup as shown in Fig. 1(a) but *without the IS*. The optical power is insufficient to produce meaningful intensity fluctuations, as these are overwhelmed by the electronic noise of the detector. Based on this

experimental observation, it is reasonable to assume that without the IS, the MI would be largely lost due to scattering.

An intuitive explanation of how an IS mitigates scattering can be provided as follows. Because of the diffuser, the probe photons are scattered nearly uniformly in all directions, covering a solid angle of 4π steradians. By placing an IS *immediately* after the diffuser, the forward-scattered probe photons from all directions are effectively recollected by the IS. These photons then undergo multiple reflections on the inner spherical surface of the IS before escaping through the exit port and eventually being focused on the photodiode. Due to these multiple reflections, a time delay ($\tau_0 = 32.7$ ns) in the MI peak relative to the unobstructed MI is observed. Additionally, due to the inner surface of the IS having a reflectivity of approximately 98%, some probe photons are inevitably lost. This results in a degraded MI peak, which is 47.5% of the unobstructed MI peak.

B. Mutual information of split conjugate beams and split coherent beams

Since the probe beam contains both the coherent “seed” photons and the thermal-like probe photons generated by the FWM process [26]. Consequently, the probe beam, as well as the conjugate beam, exhibit a mixed statistical nature with convolved coherent-light (Poisson) and thermal-light (Bose-Einstein) distributions. Therefore, the second-order correlation function $g^{(2)}$ for the probe and conjugate beams would lie between 1 and 2, where $g^{(2)} = 1$ corresponds to coherent light and $g^{(2)} = 2$ corresponds to thermal light. The measured $g^{(2)}$ values for our probe and conjugate beams are 1.146 ± 0.012 and 1.238 ± 0.011 , respectively. Since the conjugate beam exhibits the most thermal-like behavior, we therefore use the “split conjugate” beams for comparison to demonstrate the amount of MI residing in two *classically* correlated beams.

We use a $\lambda/2$ -wave plate in conjunction with a PBS to split the conjugate beam, so that the two outputs of the PBS have the same optical power as the unobstructed twin beams. Neither the scatterer nor the IS is present on the beam paths. We plot the intensity fluctuations of the two split conjugate beams in Fig. 3(a). The MI of the split conjugate beams is plotted in Fig. 3(c) as the magenta curve. As can be seen from Fig. 3(a), although the two split conjugate beams clearly exhibit correlated fluctuations, they are visibly *smoother* than the fluctuations of the unobstructed twin beams shown in Fig. 2(a), indicating a lack of high-frequency (i.e., shot-noise limited) correlations between the split conjugate beams, which is manifested by the significantly lowered peak height of the magenta curve relative to the red curve in Fig. 3(c). Also note that since there is no IS present in the split conjugate beams, the peak of the magenta curve lines up quite well with the peak of the red curve. The additional MI peak height of the twin beams compared to the split conjugate beams indicates the presence of quantum correlations in the twin beams *beyond the classical correlations* in the split conjugate beams.

We also apply identical procedures to measure the MI between two split coherent beams. The intensity fluctuations of the split coherent beams are shown in Fig. 3(b): since there are no appreciable correlations exhibited in the shot-noise-limited frequency regime, it hence gives rise to close to zero MI, represented by the blue curve in Fig. 3(c).

Note that in this work, the temporal quantum correlations are generated in the CW regime from a seeded FWM process in ^{85}Rb atomic vapor. These correlations are centered on the ^{85}Rb D₁ line and exhibit a spectral width of approximately 10 MHz [4,15]. However, as noted in Ref. [30], when using a pulsed laser, the repetition rate must be slow enough to allow the duty cycle to accommodate the exponential decay of the input pulse, which is influenced by the geometry of the IS. For both CW and pulsed lasers, the bandwidth consideration is crucially linked to

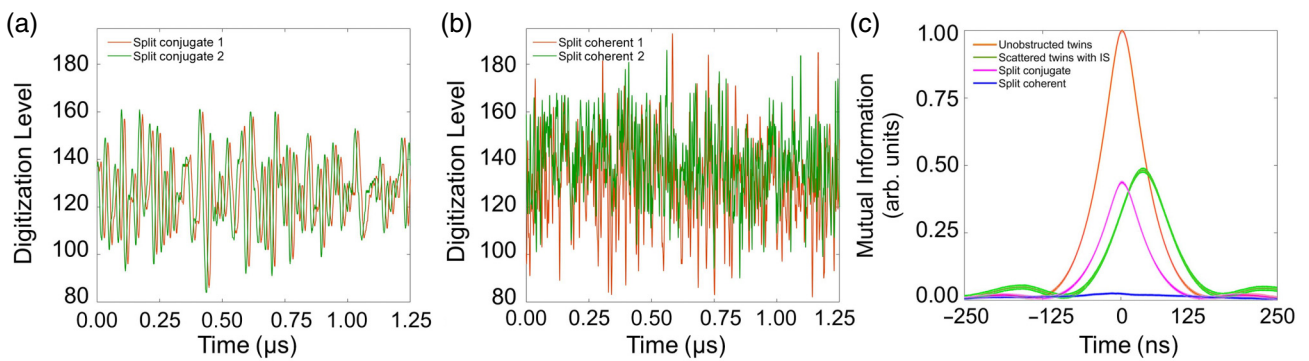


FIG. 3. (a) The intensity fluctuations of the split conjugate beams. (b) The intensity fluctuations of the split coherent beams. (c) The magenta and blue curves are the MI of the split conjugate beams and split coherent beams, respectively. They are plotted at the top of Fig. 2(c) for comparison. The shadow on each curve represents one standard deviation of averaging over ten pairs of intensity fluctuations.

the reflectivity of the inner surface of the IS. Ensuring that the bandwidth of the input light matches the spectral response of the high reflectivity of the IS is a key condition for our scattering-mitigation scheme to work effectively. We therefore attribute the main limitation of our scheme to the imperfect reflectivity of the inner surface of the IS. While the single-pass reflectivity is 98%, multiple reflections from the surface induce significant overall photon loss. We anticipate that using an IS with near-unity inner-surface reflectivity would significantly improve our current MI-recovery performance from 47.5% to a substantially higher value.

IV. THEORETICAL ANALYSIS

Our theoretical analysis for the experimental observations is shown in Fig. 2(c), based upon the assumption that the unobstructed two-mode squeezed state is Gaussian, i.e., it can be described by a Gaussian Wigner function [14,17,31]. We thus fit the MI of the unobstructed twin beams, i.e., the red curve shown in Fig. 2(c), using a Gaussian function [17,28,31]:

$$g(t) = \exp\left(-\frac{t^2}{2\sigma_0^2}\right), \quad (2)$$

where σ_0 determines the theoretical value of the FWHM of the red curve, which is given by $2\sqrt{2\ln 2}\sigma_0$. The Gaussian fit expressed by Eq. (2) is shown in Fig. 4(a) as the purple curve, from which we obtain $\sigma_0 = 32.1$ ns.

After passing through the diffuser, probe photons scattered in all directions go through Lambertian diffusive reflections on the inner surface of the IS many times before a fraction eventually escape from the IS through its apertures. These repeated random reflections give rise to a random delay in the arrival of the scattered probe photons at the exit aperture of the IS. A detailed theoretical analysis of the IS is presented in Ref. [30], which includes calculations of the temporal response of the IS and experimental results on the transformation of a pulse by the IS. The study indicates that the reflectivity of the inner surface of the IS is nearly unity (98%) and that the output pulse can be described by convolving the input with an *exponential* distribution. Our theoretical modeling of the MI data is based on these key characteristics of the IS. The parameters of our theoretical model are determined by the design of the IS and we extract these parameters from our data. We hence write the MI of the output probe and conjugate beams as

$$G(t) = \eta \int_{-\infty}^{+\infty} g(t - \tau)p(\tau) d\tau, \quad (3)$$

where η is the forward-scattering efficiency of the diffuser (as opposed to backward scattering) and $p(\tau)$ is the characteristic temporal function for the system composed of a

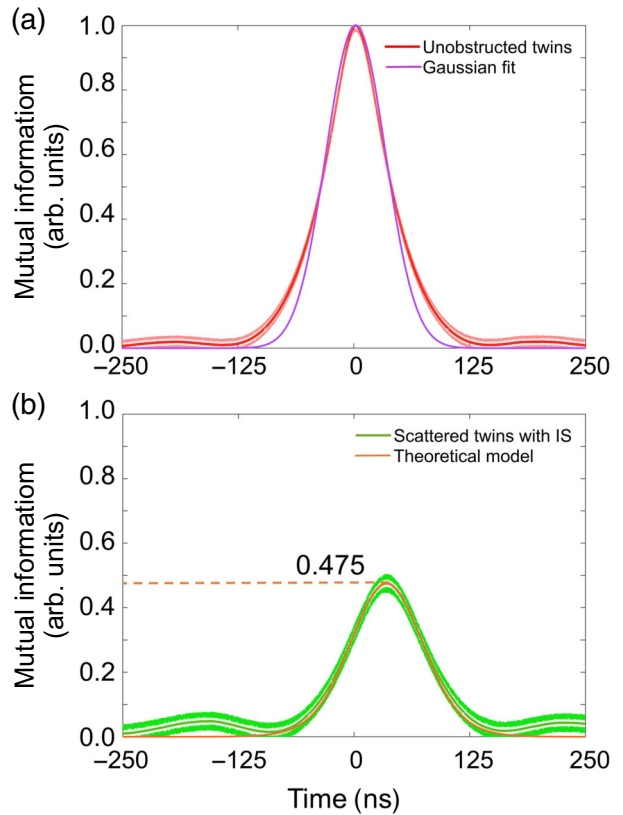


FIG. 4. (a) The Gaussian fit described by Eq. (2), shown as the purple curve. (b) The theoretical model described by Eq. (5), shown as the orange curve. The red and green curves are the same experimental data as shown in Fig. 2(c). Both the Gaussian fit and the theoretical model are in good agreement with the experimental data.

scatterer and an IS, featuring an exponential distribution according to Ref. [30]:

$$p(\tau) = \frac{1}{2\sigma} \exp\left[-\frac{|\tau - \tau_0|}{\sigma}\right]. \quad (4)$$

Here, τ_0 and σ are the average and uncertainty of the temporal delay, respectively. We have three unknown parameters, η , τ_0 , and σ , which need to be fixed from measurement data. We first note that using Eqs. (2) and (4), the function G in Eq. (3) can be analytically evaluated in terms of the error function $\text{erf}(x) = (2/\sqrt{\pi}) \int_0^x \exp(-t^2) dt$:

$$\begin{aligned} G(T) &= \frac{\eta\sigma_0\sqrt{2\pi}}{4\sigma} \exp\left(\frac{\sigma_0^2}{2\sigma^2}\right) \\ &\times \left[\exp\left(-\frac{T}{\sigma}\right) \text{erfc}\left(\frac{\sigma_0^2 - T\sigma}{\sqrt{2\sigma\sigma_0}}\right) \right. \\ &\left. + \exp\left(\frac{T}{\sigma}\right) \text{erfc}\left(\frac{\sigma_0^2 + T\sigma}{\sqrt{2\sigma\sigma_0}}\right) \right], \end{aligned} \quad (5)$$

where $T = t - \tau_0$ and $\text{erfc}(x) = 1 - \text{erf}(x)$. The parameter τ_0 is obtained from the peak-position shift in Fig. 2(c), with the value 32.7 ns. The peak value is given by

$$G(t = \tau_0) = \frac{\eta\sigma_0\sqrt{2\pi}}{2\sigma} \exp\left(\frac{\sigma_0^2}{2\sigma^2}\right) \left[1 - \text{erf}\left(\frac{\sigma_0}{\sqrt{2}\sigma}\right)\right]. \quad (6)$$

The ratio $G(t - \tau_0)/G(t = \tau_0)$ can be used to fit the line width of the green curve in Fig. 2(c). The experimental line width is 93.5 ns and this is fitted by choosing $\sigma = 19.7$ ns in $G(t - \tau_0)/G(t = \tau_0)$. Now, η can be determined from the height of the green curve, which is 0.475. This calculation yields the value of $\eta = 59.8\%$. A greater than 50% forward-scattering efficiency η is expected, as a fiber coupler mounted on a 0.5-in. polished surface is used to hold the diffuser in place at the entrance aperture of the IS. Thus, probe photons are more likely to be scattered in the forward direction than in the backward direction. The theoretical model described by Eq. (5) is plotted as the orange curve in Fig. 4(b) and is in excellent agreement with the experimental data.

V. CONCLUSIONS

We present an experimental scheme that can mitigate the adverse effect of scattering on quantum correlations in a quantum system. We use the MI as the information metric to quantify quantum correlations in our system, which consists of a two-mode squeezed state with 7-dB intensity-difference squeezing, generated by the FWM process in atomic ^{85}Rb vapor. Our mitigation scheme involves only an IS and we demonstrate a 47.5% MI recovery from scattering after 32.7 ns of information-storage time, despite experiencing an enormous photon loss of greater than 85%.

Since scattering can contribute to both decoherence and loss—the two main disruptive random processes in quantum systems—our scheme can thus be found useful in many circumstances in which disruptive random processes are unavoidable, paving the way for implementing delicate QISE protocols in real-life situations. For instance, in quantum communication systems, scattering can cause quantum signals to deviate from their intended path or degrade in fidelity. Mitigating scattering helps maintain the coherence and integrity of quantum signals over long-distance communication channels, such as in quantum key distribution [32] or teleportation protocols [33]. In quantum computing platforms, where delicate qubits are manipulated, scattering can introduce errors by prematurely decohering qubits [34]. Therefore, mitigating scattering effects is essential for improving the stability and coherence times of qubits, thereby enhancing the overall computational performance of quantum algorithms [35]. In quantum sensing systems, scattering can obstruct precise measurement techniques that rely on quantum states [36].

For example, in quantum metrology using interferometric methods, minimizing scattering effects ensures accurate signal detections, thereby reliably improving the sensitivity of quantum sensors [37].

ACKNOWLEDGMENTS

The experiment was performed under the supervision of T.L. in his quantum sensing laboratory at the University of Tennessee at Chattanooga. Z.J. is supported by the Herman F. Heep and Minnie Belle Heep Texas A&M University Endowed Fund held and administered by the Texas A&M Foundation. We would like to thank the Robert A. Welch Foundation (Grants No. A-1261, A-1547 and No. A-1943), the Air Force Office of Scientific Research (Award No. FA9550-20-1-0366), and the National Science Foundation (Grant No. PHY-2013771). This material is also based on work supported by the U.S. Department of Energy, Office of Science under Award No. DE-AC36-08GO28308, and Office of Biological and Environmental Research under Award No. DE-SC-0023103 and Award No. 500.

- [1] M. A. Nielsen and I. L. Chuang, *Quantum Computation and Quantum Information* (Cambridge University Press, Cambridge, 2010).
- [2] E. Joos, H. D. Zeh, C. Kiefer, D. J. Giulini, J. Kupsch, and I.-O. Stamatescu, *Decoherence and the Appearance of a Classical World in Quantum Theory* (Springer Science & Business Media, Heidelberg, 2013).
- [3] H.-A. Bachor and T. C. Ralph, *A Guide to Experiments in Quantum Optics* (John Wiley & Sons, Weinheim, 2019).
- [4] T. Li, F. Li, X. Liu, V. V. Yakovlev, and G. S. Agarwal, Quantum-enhanced stimulated brillouin scattering spectroscopy and imaging, *Optica* **9**, 959 (2022).
- [5] C. A. Casacio, L. S. Madsen, A. Terrasson, M. Waleed, K. Barnscheidt, B. Hage, M. A. Taylor, and W. P. Bowen, Quantum-enhanced nonlinear microscopy, *Nature* **594**, 201 (2021).
- [6] R. B. de Andrade, H. Kerdoncuff, K. Berg-Sørensen, T. Gehring, M. Lassen, and U. L. Andersen, Quantum-enhanced continuous-wave stimulated Raman scattering spectroscopy, *Optica* **7**, 470 (2020).
- [7] B. J. Lawrie, P. D. Lett, A. M. Marino, and R. C. Pooser, Quantum sensing with squeezed light, *Acs Photonics* **6**, 1307 (2019).
- [8] Y. Michael, L. Bello, M. Rosenbluh, and A. Pe'er, Squeezing-enhanced Raman spectroscopy, *npj Quantum Inf.* **5**, 81 (2019).
- [9] J. B. Clark, F. Lecocq, R. W. Simmonds, J. Aumentado, and J. D. Teufel, Observation of strong radiation pressure forces from squeezed light on a mechanical oscillator, *Nat. Phys.* **12**, 683 (2016).
- [10] J. Aasi, J. Abadie, B. Abbott, R. Abbott, T. Abbott, M. Abernathy, C. Adams, T. Adams, P. Addesso, R. Adhikari, *et al.*, Enhanced sensitivity of the LIGO gravitational wave detector by using squeezed states of light, *Nat. Photonics* **7**, 613 (2013).

- [11] M. A. Taylor, J. Janousek, V. Daria, J. Knittel, B. Hage, H.-A. Bachor, and W. P. Bowen, Biological measurement beyond the quantum limit, *Nat. Photonics* **7**, 229 (2013).
- [12] S. L. Braunstein and P. Van Loock, Quantum information with continuous variables, *Rev. Mod. Phys.* **77**, 513 (2005).
- [13] C.-H. Wu, C.-K. Liu, Y.-C. Chen, and C.-S. Chuu, Revival of quantum interference by modulating the biphotons, *Phys. Rev. Lett.* **123**, 143601 (2019).
- [14] A. Serafini, F. Illuminati, and S. De Siena, Symplectic invariants, entropic measures and correlations of Gaussian states, *J. Phys. B: At. Mol. Opt. Phys.* **37**, L21 (2003).
- [15] J. B. Clark, R. T. Glasser, Q. Glorieux, U. Vogl, T. Li, K. M. Jones, and P. D. Lett, Quantum mutual information of an entangled state propagating through a fast-light medium, *Nat. Photonics* **8**, 515 (2014).
- [16] U. Vogl, R. T. Glasser, J. B. Clark, Q. Glorieux, T. Li, N. V. Corzo, and P. D. Lett, Advanced quantum noise correlations, *New J. Phys.* **16**, 013011 (2014).
- [17] C. Weedbrook, S. Pirandola, R. García-Patrón, N. J. Cerf, T. C. Ralph, J. H. Shapiro, and S. Lloyd, Gaussian quantum information, *Rev. Mod. Phys.* **84**, 621 (2012).
- [18] V. Ameri, M. Eghbali-Arani, A. Mari, A. Farace, F. Kheirandish, V. Giovannetti, and R. Fazio, Mutual information as an order parameter for quantum synchronization, *Phys. Rev. A* **91**, 012301 (2015).
- [19] P. B. Dixon, G. A. Howland, J. Schneeloch, and J. C. Howell, Quantum mutual information capacity for high-dimensional entangled states, *Phys. Rev. Lett.* **108**, 143603 (2012).
- [20] M. M. Wolf, F. Verstraete, M. B. Hastings, and J. I. Cirac, Area laws in quantum systems: Mutual information and correlations, *Phys. Rev. Lett.* **100**, 070502 (2008).
- [21] V. P. Belavkin and M. Ohya, Entanglement, quantum entropy and mutual information, *Proc. R. Soc. Lond. Ser. A: Math. Phys. Eng. Sci.* **458**, 209 (2002).
- [22] M. Dowran, A. Kumar, B. J. Lawrie, R. C. Pooser, and A. M. Marino, Quantum-enhanced plasmonic sensing, *Optica* **5**, 628 (2018).
- [23] B. E. Anderson, P. Gupta, B. L. Schmittberger, T. Horrom, C. Hermann-Avigliano, K. M. Jones, and P. D. Lett, Phase sensing beyond the standard quantum limit with a variation on the SU(1,1) interferometer, *Optica* **4**, 752 (2017).
- [24] R. C. Pooser and B. Lawrie, Ultrasensitive measurement of microcantilever displacement below the shot-noise limit, *Optica* **2**, 393 (2015).
- [25] F. Hudelist, J. Kong, C. Liu, J. Jing, Z. Ou, and W. Zhang, Quantum metrology with parametric amplifier-based photon correlation interferometers, *Nat. Commun.* **5**, 3049 (2014).
- [26] F. Li, T. Li, and G. S. Agarwal, Experimental study of decoherence of the two-mode squeezed vacuum state via second harmonic generation, *Phys. Rev. Res.* **3**, 033095 (2021).
- [27] T. Li, B. E. Anderson, T. Horrom, B. L. Schmittberger, K. M. Jones, and P. D. Lett, Improved measurement of two-mode quantum correlations using a phase-sensitive amplifier, *Opt. Express* **25**, 21301 (2017).
- [28] U. Vogl, R. T. Glasser, Q. Glorieux, J. B. Clark, N. V. Corzo, and P. D. Lett, Experimental characterization of Gaussian quantum discord generated by four-wave mixing, *Phys. Rev. A* **87**, 010101 (2013).
- [29] T. Li, F. Li, C. Altuzarra, A. Classen, and G. S. Agarwal, Squeezed light induced two-photon absorption fluorescence of fluorescein biomarkers, *Appl. Phys. Lett.* **116**, 254001 (2020).
- [30] E. S. Fry, J. Musser, G. W. Kattawar, and P.-W. Zhai, Integrating cavities: Temporal response, *Appl. Opt.* **45**, 9053 (2006).
- [31] L.-M. Duan, G. Giedke, J. I. Cirac, and P. Zoller, Inseparability criterion for continuous variable systems, *Phys. Rev. Lett.* **84**, 2722 (2000).
- [32] R. Valivarthi, M. I. G. Puigibert, Q. Zhou, G. H. Aguilar, V. B. Verma, F. Marsili, M. D. Shaw, S. W. Nam, D. Oblak, and W. Tittel, Quantum teleportation across a metropolitan fibre network, *Nat. Photonics* **10**, 676 (2016).
- [33] Q.-H. Lu, F.-X. Wang, K. Huang, X. Wu, Z.-H. Wang, S. Wang, D.-Y. He, Z.-Q. Yin, G.-C. Guo, W. Chen, *et al.*, Quantum key distribution over a channel with scattering, *Phys. Rev. Appl.* **17**, 034045 (2022).
- [34] H. G. Krojanski and D. Suter, Reduced decoherence in large quantum registers, *Phys. Rev. Lett.* **97**, 150503 (2006).
- [35] M. Schlosshauer, Quantum decoherence, *Phys. Rep.* **831**, 1 (2019).
- [36] Y. Matsuzaki, S. C. Benjamin, and J. Fitzsimons, Magnetic field sensing beyond the standard quantum limit under the effect of decoherence, *Phys. Rev. A—At. Mol. Opt. Phys.* **84**, 012103 (2011).
- [37] M. A. Taylor and W. P. Bowen, Quantum metrology and its application in biology, *Phys. Rep.* **615**, 1 (2016).